

Article

Promoter Impact on 5Ni/SAPO-5 Catalyst for H₂ Production via Methane Partial Oxidation

Abdulaziz Al-Anazi ¹, Omer Bellahwel ¹, Kavitha C. ², Jihad Abu-Dahrieh ^{3,*}, Ahmed A. Ibrahim ¹, S. Santhosh ², Ahmed E. Abasaheed ¹, Anis H. Fakeeha ¹ and Ahmed S. Al-Fatesh ^{1,*}

¹ Department of Chemical Engineering, College of Engineering, King Saud University (KSU), P.O. Box 800, Riyadh 11421, Saudi Arabia; aalanazi15@ksu.edu.sa (A.A.-A.); bellahwel000@gmail.com (O.B.); aidid@ksu.edu.sa (A.A.I.); abasaheed@ksu.edu.sa (A.E.A.); anishf@ksu.edu.sa (A.H.F.)

² Department of Chemistry, Dwaraka Doss Goverdhan Doss Vaishnav College (Autonomous), University of Madras, 833, Gokul Bagh, EVR Periyar Road, Arumbakkam, Chennai 600106, India; kavithakandhan@gmail.com (K.C.); santhoshsgp03@gmail.com (S.S.)

³ School of Chemistry and Chemical Engineering, Queen's University Belfast, Belfast BT9 5AG, UK

* Correspondence: j.abudahrieh@qub.ac.uk (J.A.-D.); aalfatesh@ksu.edu.sa (A.S.A.-F.)

Abstract: Compared to steam reforming techniques, partial oxidation of methane (POM) is a promising technology to improve the efficiency of synthesizing syngas, which is a mixture of CO and H₂. In this study, partial oxidation of methane (POM) was used to create syngas, a combination of CO and H₂, using the SAPO-5-supported Ni catalysts. Using the wetness impregnation process, laboratory-synthesized Ni promoted with Sr, Ce, and Cu was used to modify the SAPO-5 support. The characterization results demonstrated that Ni is appropriate for the POM due to its crystalline structure, improved metal support contact, and increased thermal stability with Sr, Ce, and Cu promoters. During POM at 600 °C, the synthesized 5Ni+1Sr/SAPO-5 catalyst sustained stability for 240 min on stream. While keeping the reactants stoichiometric ratio of (CH₄:O₂ = 2:1), the addition of Sr promoter and active metal Ni to the SAPO-5 increased the CH₄ conversion from 41.13% to 49.11% and improved the H₂/CO ratio of 3.33. SAPO-5-supported 5Ni+1Sr catalysts have great potential for industrial catalysis owing to their unique combination of several oxides. This composition not only boosts the catalyst's activity but also promotes favorable physiochemical properties, resulting in improved production of syngas. Syngas is a valuable intermediate in various industrial processes.

Keywords: partial oxidation; methane; syngas; 5Ni+1Sr/SAPO-5; crystalline structure



Citation: Al-Anazi, A.; Bellahwel, O.; C., K.; Abu-Dahrieh, J.; Ibrahim, A.A.; Santhosh, S.; Abasaheed, A.E.; Fakeeha, A.H.; Al-Fatesh, A.S. Promoter Impact on 5Ni/SAPO-5 Catalyst for H₂ Production via Methane Partial Oxidation. *Catalysts* **2024**, *14*, 316. <https://doi.org/10.3390/catal14050316>

Academic Editor: Antonio Vita

Received: 30 March 2024

Revised: 5 May 2024

Accepted: 7 May 2024

Published: 10 May 2024



Copyright: © 2024 by the authors. Licensee MDPI, Basel, Switzerland. This article is an open access article distributed under the terms and conditions of the Creative Commons Attribution (CC BY) license (<https://creativecommons.org/licenses/by/4.0/>).

1. Introduction

Fossil fuels are the primary supplier of energy, and global energy consumption is growing constantly [1]. Considering fossil fuel has the greatest pace of expansion, natural gas is projected to satisfy this rising requirement and currently serves as the world's second-largest energy provider after coal. Electricity, as well as heat, originate directly from natural gas [2]. However, the largest natural gas deposits are located offshore or in remote locations far away from industrial zones. This substantially impacts both the monetary value of natural gas and geopolitical issues. In addition, the fact that natural gas is a gas at ambient temperature might make storage and transportation difficult [3]. This has led scientists all around the world to explore different ways to harness methane (CH₄), the main component of natural gas, more effectively. Although CH₄ is widely used in a variety of applications, including solid oxide fuel cells [4], the combustion process, and other processing applications [5], it is primarily employed in the synthesis of various organic substances, including methanol, formaldehyde, and other hydrocarbons. However, the primary hurdles associated with CH₄ arise from its high degree of reactivity as well as its poor selectivity. Manufacturing syngas, a blend of H₂ and CO, from CH₄ constitutes one of the finest and most cost-effective uses of the gas [6,7]. It is used in the manufacturing

sector as an essential precursor and combustibility source for the synthesis of gaseous fuels, liquid fuels, and various chemicals. POM is a highly promising method for methane conversion, offering high conversion efficiency, selectivity, and short residence times [8,9]. It can proceed via direct or indirect mechanisms, with the former being more efficient and cost-effective [10]. However, challenges such as catalyst deactivation due to metal sintering, hotspot formation, and coke deposition remain unresolved. To address these challenges, researchers have explored a variety of catalysts, including transition metals, noble metals, and perovskites. Mixed metal oxides and waste-derived catalysts have also shown promise in improving catalytic performance and stability [11–13]. Recent studies have focused on optimizing catalyst composition, morphology, and support materials to enhance catalytic activity and stability. For example, loading Ni on La₂O₃ has demonstrated excellent stability and activity, attributed to favorable metal-support interactions and reduced coke formation [14]. Similarly, Co-supported Yb₂O₃ has shown increased conversion rates and stability in POM reactions [15]. Perovskite-based catalysts have received considerable attention for their high activity and thermal stability, making them promising candidates for methane conversion [16]. Waste-derived catalysts, such as Co/CeO₂-BFA and CaO from eggshells, offer cost-effective alternatives to conventional catalysts. Co/CeO₂-BFA has been employed for methane decomposition, leveraging various oxides present in the waste material to improve catalytic activity [17]. CaO, with its low cost and strong basic nature, has shown high catalytic activity in methane conversion. However, challenges such as catalyst deactivation due to water adsorption and low surface area restrict their widespread utilization [18,19]. Also, there are significant advancements in the partial oxidation of methane (POM) using metals supported by MgO, CeO₂, ZrO₂, and FeO₂. Short contact time vessels operating adiabatically have been employed, reducing reactor complexity and dimensions, thus lowering capital expenditure. These vessels, with contact times of 0.01 s or lower, eliminate the need for a furnace but require moderate preheating. Additionally, they result in lower CO₂ emissions compared to steam methane reforming (SMR) burners, which contribute significantly to global CO₂ emissions. Ni-Ru/CeO₂ species deposited on a FeCrAl gauze have also been used as POM catalysts, Ni with the support precursor and pretreatment conditions significantly influencing catalytic performance showed the highest selectivity to syngas, with a H₂/CO ratio close to 2.0 [20].

Numerous catalyst schemes have been experimentally proposed for POM since the conversion of CH₄ to syngas additionally calls for high temperatures, even if there is a lack of catalyst involved [21]. Currently, the vast majority of industrial synthesis requires catalysts as well; hence, research into materials with catalytic properties is critical for the creation of appropriate catalysts [22]. In heterogeneous catalysis, the majority of appropriate catalysts are made up of active component(s) and support materials. In general, catalyst backbones have been used for housing the active components, strengthening the active site's dispersion, a particular amount of surface area, and stability [23,24]. The most important variables determining the eligibility of support structures for catalysts are specific surface area, porosity, particle size and shape, and mechanical and thermal resistance [25]. The aforementioned substances are particularly useful in manufacturing processes such as reforming methane with steam and catalytic partial oxidation of methane using supports [26]. As a result, establishing novel or modified synthesis pathways is critical for lowering the cost of these support materials or strengthening their key properties [27].

The ultimate objective of this research is to create small, nano-crystalline structures of SAPO-5-supported on Ni promoted with Sr, Ce, and Cu catalysts for low-temperature, coking-free partial oxidation of methane reactions. Our SAPO-5-supported catalyst was synthesized with various Ni with Sr/Ce/Cu concentrations, utilizing the well-known wetness impregnation process to optimize the Ni with Sr/Ce/Cu content and calcination temperature. The catalyst was calcined at 600 °C to improve its crystallinity. The partial oxidizing of the methane process was evaluated at 600 °C to evaluate performance and find the lowest reaction temperature with the greatest CH₄ conversion, excellent H₂/CO selectivity, and stability. The effectiveness and durability of the best-optimized 5Ni+1Sr/SAPO-5

catalyst samples were investigated further. The factors responsible for outstanding catalytic activity and stable performance were explored utilizing fresh and spent catalyst characterization techniques such as XRD, FTIR, BET TEM, Raman, and TPD-NH₃. The crucial function of oxygen within the lattice and metal-support interaction in determining catalytic activity and stability was explored.

2. Catalyst Characterization

2.1. X-ray Diffraction Analysis

Figure 1A shows the high-degree X-ray diffraction spectra of 5Ni/SAPO-5, 5Ni+1Sr/SAPO-5, 5Ni+1Cu/SAPO-5, and 5Ni+1Ce/SAPO-5. It can be observed from the figure that there is a good resemblance in the location of peaks for 5Ni/SAPO-5 and other samples. This shows the similarity in the crystallization of the samples. The X-ray diffraction (XRD) patterns display major peaks at 7.41° (100), 14.70° (200), 19.61° (210), 20.68° (002), 22.23° (211), and 25.84° (220), indicating the phase purity of SAPO-5 in all samples. These peaks are well indexed by the standard hexagonal crystal phase with space group p6/mmc [28]. An intense (100) peak was observed at a diffraction angle, 2θ located at 7.5°, which is attributed to the significant growth of the crystal plane (100) located at 7.5°. The atoms are thus arranged in this preferred plane orientation (100), and the intense peak (100) is accompanied by peaks between 12.5° and 37.5° to minimize the surface energy. Interestingly, X-ray diffraction analysis did not detect any characteristic peaks for nickel (Ni), (Ni—referencing JCPDS# 04-0835), Sr, Cu, Ce, or their related compounds within the SAPO-5 support. The lack of diffraction peaks for Ni, Ni, Sr, Cu, or Ce in the SAPO-5 samples could be due to either their low concentration or a homogenous distribution throughout the support. However, the absence of these metal-specific peaks might also indicate their successful incorporation into the framework structure of the SAPO-5, making them undetectable by conventional X-ray diffraction techniques. This indicates the absence of secondary phases in the sample. Introducing metal ions to the 5Ni/SAPO-5 samples increases the intensity of the characteristic peaks, leading to a slight increase in the relative crystallinity of the samples.

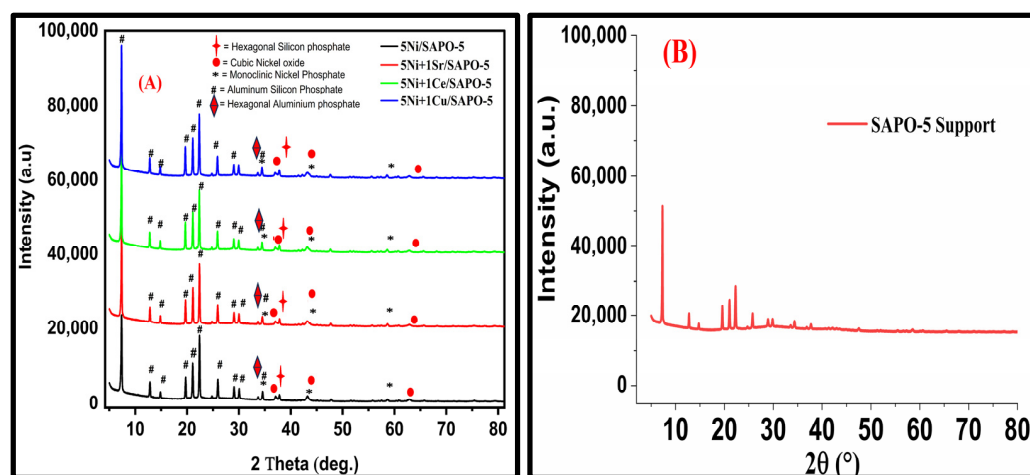


Figure 1. High angle XRD pattern of bimetallic catalyst supported on SAPO-5; (A) promoted 5Ni/SAPO-5; (B) SAPO-5 support.

The results indicate that samples containing bimetallic materials exhibit higher relative crystallinity compared to those composed of nickel and SAPO-5. This is likely due to the influence of the bimetallic loading on the crystal growth process. Additionally, by considering the inclusion of the metals in the SAPO-5 framework, distorted versions in the crystalline network can be pointed out. This is because the bond angles that link the tetrahedral construction units (MO₄ and TO₄) are altered by the variation in bond lengths that exists between the M–O and typical T–O (T ¼ = Si, Al, or P), which causes distortions throughout the crystalline framework and enhances the crystalline structure

of materials [29,30]. Additionally, it shows exactly how SAPO-5's hexagonal tendencies coincide with a hexagonal crystal structure [18,19]. Figure 1B of the support information provides the XRD pattern of the SAPO-5 catalyst support. It shows the dominance pattern of SAPO-5 over the actual active phases of catalysts.

2.2. FTIR Spectra Analysis

Figure 2 exhibits the FTIR spectra of the 5Ni/SAPO-5, 5Ni+1Sr/SAPO-5, 5Ni+1Cu/SAPO-5, and 5Ni+1Ce/SAPO-5 samples. The vibration stretching frequency of the T-O-T unit (where T is Si, Al, or P) seen in the D4R and D6R secondary construction units is represented by the bands at 553 and 630 cm^{-1} in the FT-IR spectra of the catalyst samples mentioned above (Figure 2). The strong peak of about 1050 cm^{-1} is associated with the asymmetric stretching of the T-O-T unit framework (T = Si, Al, and P). Si-O-Si vibrations are responsible for the bands at about 1000 cm^{-1} , while Al-O vibrations are responsible for the bands at 704 and 746 cm^{-1} [31,32]. P-O-Al symmetric stretching vibration is symbolized by bands at 740 cm^{-1} and 820 cm^{-1} . Furthermore, the challenge was to prevent water from adhering to the crystals' channels, causing bands to form at 1647 and 1668 cm^{-1} , respectively, for the vibration of the hydroxyl groups in the water. Subsequently, bands generated at 3486 cm^{-1} and 3430 cm^{-1} , respectively, originate from interactions among Si-OH and P-OH units through hydrogen bonds. Schnabel et al. [5] report that the bands at 562 and 634 cm^{-1} can be assigned to certain lattice vibrations and are particularly sensitive to AlPO-5 and SAPO-5. The inclusion of Ni with Sr/Cu/Ce into SAPO-5 does not change the parent material's lattice structure in a way that can be determined by FTIR, as shown by the remarkably comparable spectrum (Figure 3) obtained from all samples. The lattice vibrations cannot be appreciably altered by the effectual isomorphous substitution of Ni, as the concentration of Ni is negligible. Surface enhancement, consistent with the literature, may be responsible for the shift in vibrational bands [33,34]. The aforementioned changes demonstrate that Ni is capable of being mixed with Cu, Sr, and Ce particles to form the SAPO-5 composite. Upon comparing the infrared spectra of the 5Ni/SAPO-5 and Ni with Cu/Sr/Ce, including SAPO samples (Figure 3), the following observations can be made: Both the pure 5Ni/SAPO-5 and the Ni-Cu/Sr/Ce-SAPO samples exhibit bands around 3500 cm^{-1} . In the case of Ni/SAPO-34, a comparable band at 3430 cm^{-1} was discovered and attributed to bridging hydrogen-linked species, which stabilized the nickel framework substitution in SAPO-34. We propose that the band at 3450 cm^{-1} might originate from some species of nickel. The intensity of the band at about 3625 cm^{-1} , which is attributed to acidic Si-OH-Al groups in pure SAPO-5, does not significantly alter in samples that have been changed by Ni. The wide stretching band between 3200 and 3600 cm^{-1} in the hydroxyl area (3000–4000 cm^{-1}) is attributed to connecting hydroxyl groups, Si-OH-Al, resulting in SAPO-5's Brønsted acidity [35]. Two perspectives are speculated to be the origin of this band's broad width. Specifically, two bands associated with OH may overlap, interconnecting hydroxyl groups and extending the vibrations of free water. In addition, the potent hydrogen bonding that arises from the existence of OH groups widens the OH bands and, in particular instances, substantially minimizes the stretching frequency. It ought to be mentioned that the number, as well as the strength of hydrogen bonds, vary depending on the interactions between molecules and chemical environments, resulting in half-widths for OH stretching of 300–500 cm^{-1} .

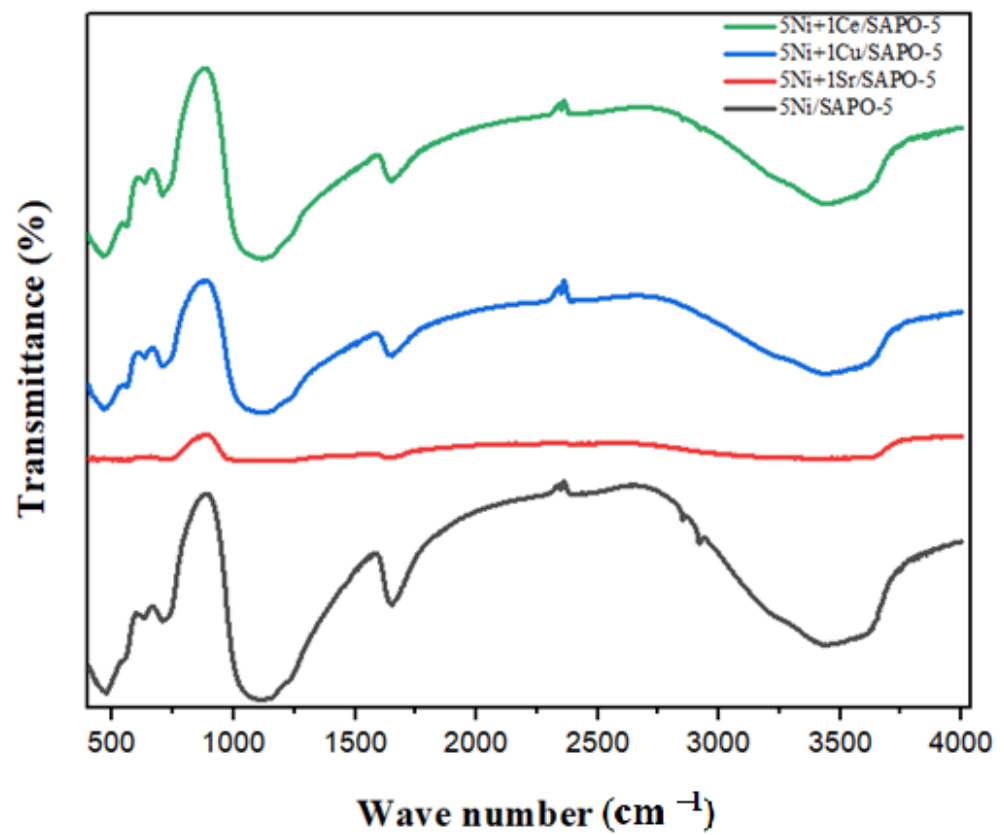


Figure 2. FT-IR spectra of bimetallic catalyst supported by SAPO-5 (5Ni/SAPO-5; 5Ni +1Sr+SAPO-5; 5Ni +1Ce/SAPO-5; 5Ni +1Cu/SAPO-5).

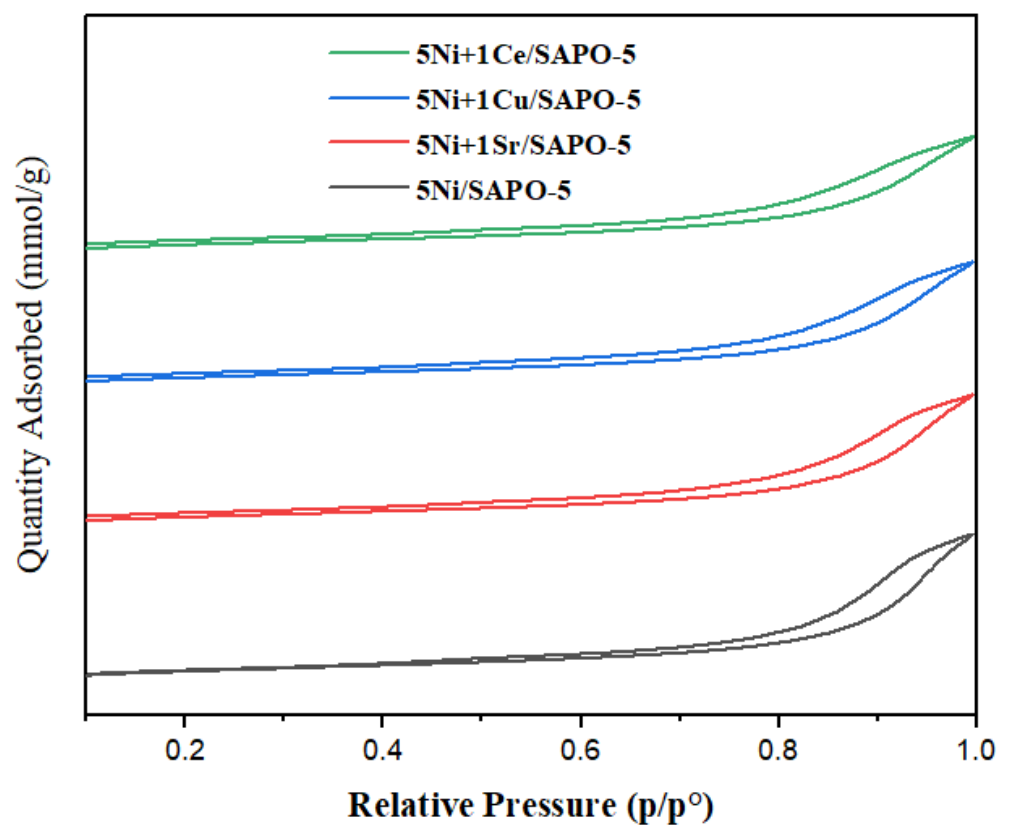


Figure 3. BET isotherm of 5Ni/SAPO-5 and 5Ni +1x/SAPO-5 (x = Sr, Cu, and Ce).

2.3. BET Adsorption and Desorption Isotherms

Each catalyst's mass-specific surface area was calculated using the BET method, and its pore size distribution was ascertained using the BJH method. The quantity of N₂ that is adsorbed and desorbed from the sample is the basis for these techniques. Table 1 contains a list of the catalyst's physical characteristics, including its mass-specific surface area, pore diameter, and pore volume. Figure 3 shows typical type-IV nitrogen adsorption–desorption isotherms with H3 hysteresis loops for all the catalysts: 5Ni, 5Ni/1Sr, 5Ni/1Cu, and 5Ni/1Ce supported on SAPO-5. This type of isotherm with an H3 loop is characteristic of mesoporous materials [36]. It often occurs in materials with non-uniform pore shapes (like clusters or clumps of particles) and slit-shaped voids (think of flakes or sharp-edged cubes). Mesopores began to form in the catalyst as a result of inter-crystalline voids created by the accumulation of nanocrystals. Moreover, the hysteresis loop produced capillary condensation in these mesopores.

Table 1 illustrates the surface area, pore volume, and pore diameter of SAPO-5 with Ni, Sr, Cu, and Ce concentrations. 5Ni/SAPO-5 has an average pore size of 7.14 nm and a specific surface area of 410.02 m² g⁻¹. The specific surface areas of 5Ni+1Sr/SAPO-5, 5Ni+1Cu/SAPO-5, and 5Ni+1Ce/SAPO-5 are 398.77, 375.60, and 340.10 m² g⁻¹, respectively, when the additional metallic element is added to the 5Ni/SAPO-5. This is because of the inclusion of Ni, which blocks the catalyst's pores through sintering and agglomeration during calcination. In the meantime, Ni agglomeration in the catalyst is inhibited by the impregnation of 1 wt.% Ce/Sr/Cu in 5Ni/SAPO-5 catalyst, which raises the surface area above that of 5Ni/SAPO-5. A high specific surface area often helps the catalytic process since it allows for the adsorption of additional reactants on active sites. The aforementioned investigations have unequivocally demonstrated that bimetallic inclusion affects the textural properties of Ni supported on SAPO-5. Consequently, the addition of Ce/Sr/Cu leads to a reduction in the mean pore diameter, and the entire surface area is reduced [37]. Multilayer progression is brought about by mesopore adsorption at high relative pressures. However, condensation begins when the pressure surpasses a particular value, which is established by Kelvin-type equations (higher pressure for larger mesopores), leading to an abrupt rise in the adsorption volume. Conversely, the addition of bimetallic groups reduced the catalysts' specific surface area and obstructed their pores in the following order: 5Ni+1Sr/SAPO-5 > 5Ni+1Cu/SAPO-5 > 5Ni+1Ce/SAPO-5. This is because SAPO-5's interfacial contact between different metals can produce an uneven surface area while increasing the number of contact points [5]. More active sites for gas adsorption were provided by the increased surface area, which also increased the reactant molecules' accessibility to the catalyst surface and increased catalytic activity. The SAPO-5 support indicates a decrease in BET surface due to the impregnation of the active metal oxides.

Table 1. Surface areas and pore volumes of the catalysts.

| Catalyst | S _{BET} (m ² /g) ^a | Pore Volume (cm ³ /g) ^b | Dp (nm) ^c | Acid Sites (mmol NH ₃ /g Catalyst) (Weak) | Acid Sites (mmol NH ₃ /g Catalyst) (Strong) | Total Acidity (mmol NH ₃ /g Catalyst) |
|----------------|--|--|-------------------------|--|---|--|
| SAPO-5 | 247 | 0.19 | 1.41 | - | - | - |
| 5Ni/SAPO-5 | 241 | 0.17 | 7.14 | 0.48 | 0.55 | 1.03 |
| 5Ni+1Sr/SAPO-5 | 168 | 0.15 | 7.05 | 0.69 | 0.96 | 1.65 |
| 5Ni+1Cu/SAPO-5 | 194 | 0.14 | 7.00 | 0.70 | 0.86 | 1.56 |
| 5Ni+1Ce/SAPO-5 | 209 | 0.13 | 6.67 | 0.73 | 0.78 | 1.51 |

^a Measured by the t-plot method. ^b V_{meso} = V_{total} – V_{micro}. ^c BJH Adsorption average pore width (4V/A) method*LT.

2.4. Temperature Programmed Reduction

The reducibility of the catalyst as well as its capacity for H₂ diffusion into the catalyst were assessed through H₂-TPR. Although the synthesized catalyst is in metal oxide form,

the POM requires metallic Ni (Ni^0) as the active phase; hence, the H_2 -TPR investigation is of extreme importance as it guides the best way to activate the catalyst before evaluating its efficacy. Figure 4 compares the H_2 -TPR patterns for the catalysts that are 5Ni/SAPO-5, 5Ni+1Sr/SAPO-5, 5Ni+1Cu/SAPO-5, and 5Ni+1Ce/SAPO-5. The analysis revealed two separate reduction peaks: one began at 300 °C and terminated at 720 °C, while the other was spotted at a higher temperature. In the case of 5Ni/SAPO-5, the scattered nickel was anticipated to be responsible for the higher temperature reduction peak, whereas the reduction of substantial nickel oxide entities with less contact with SAPO-5 was accountable for the lower one [38]. Furthermore, the reduction of nickel aluminate (NiAl_2O_4) may be associated with the reduction peak observed at temperatures exceeding 900 °C. The maximal hydrogen consumption for 5Ni+1Sr/SAPO-5 and 5Ni+1Ce/SAPO-5 was found to be 652 °C, and this was attributed to the reduction of Ni, Sr, and Ce. Two reduction peaks were seen in area I of the TPR profile for Sr or Ce on 5Ni/SAPO-5, one at 320 °C and the next shoulder peak at 430 °C. The reduction of Sr or Ce was accountable for the subsequent peak, while the reduction of nickel oxide was the cause of the former peak [39]. Remarkably, the 5Ni+Sr/SAPO-5 reduction peak in the area I relocated slightly to the lower temperature side in contrast to the 5Ni+Ce/SAPO-5 reduction peak.

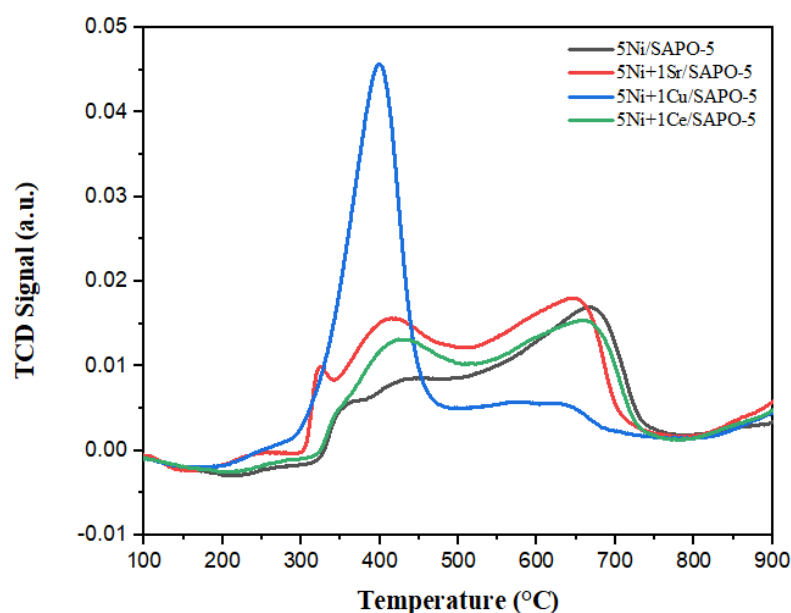


Figure 4. Temperature Programmed Reduction of 5Ni/SAPO-5 and 5Ni +1x/SAPO-5 (x = Sr, Cu, and Ce).

The hydrogen spillover from nickel to strontium explains this outcome. On the other hand, as the reduction temperature increased, the reduction degree of Ni/SAPO-5 and 5Ni+Ce/SAPO-5 showed a propensity to continuously increase. The literature states that the highly dispersed copper oxide occurring on the surface, isolated copper ions, and compact two- and three-dimensional clumps are the root causes of the high-intensity pattern recognized for 5Ni+1Cu/SAPO-5 [40]. Furthermore, Figure 4 exhibits that peak temperatures and the TCD signal persist intact and overlap between the peaks while Sr or Ce were inserted on 5Ni/SAPO-5. This implies that the reducibility of the maxima of cerium oxide and strontium oxide species is not significantly different from 5Ni/SAPO-5. 5Ni+Cu/SAPO-5 can only be attributed to the reduction of the isolated Cu^+ ions that are produced during the low-temperature reduction process, as the peak emerges at a higher temperature. The maxima of the peaks shift somewhat to a lower temperature and an increase in intensity, but otherwise, they are centered at locations that are identical to those for 5Ni+Cu/SAPO-5. This means that the reduction of Cu^+ to metallic copper particles correlates with the reduction peak that shows up in the H_2 -TPR curve for 5Ni+Cu/SAPO-5 at 300–600 °C. It implies that during reduction between 200 and 300 °C, H_2 reduces all

of the isolated Cu^{2+} ions to Cu^+ . The emergence of a peak, indicative of metallic copper particles, indicates that the Cu^+ ions generated during the reduction of Cu^{2+} are further reduced to metallic Cu when the termination temperature of the TPR pre-treatments of 5Ni+Cu/SAPO-5 is raised to 400 °C and the CuO clumping on the 5Ni/SAPO-5 catalyst causes the non-existence of the Ni peak. Table S1 of the support information displays the following: H_2 uptake of the samples during TPR analysis calcined at 600 °C.

2.5. High-Resolution Transmission Electron Microscopy (HR-TEM)

Figure 5a–d shows the HR-TEM images of samples (a) 5Ni/SAPO-5, (b) 5Ni/1Sr+SAPO-5, (c) 5Ni/1Ce+SAPO-5, (d) 5Ni/1Cu+SAPO-5. In Figure 5a, the shape and morphology of Ni have been observed as quasi-spherical, with some aggregated particles of Ni [41,42]. TEM of 5Ni +1Ce/SAPO-5 (Figure 5c) was found to be in both microsphere and quasi-spherical morphology and is attributed to the presence of Ce and Ni in SAPO-5. The HR-TEM image of 5Ni+1Cu/SAPO-5 (Figure 5d) depicts the morphology of copper particles as spherical [43]. The intergrowth of cubic particles is also observed for the 5Ni/SAPO-5 sample in Figure 5a,c,d.

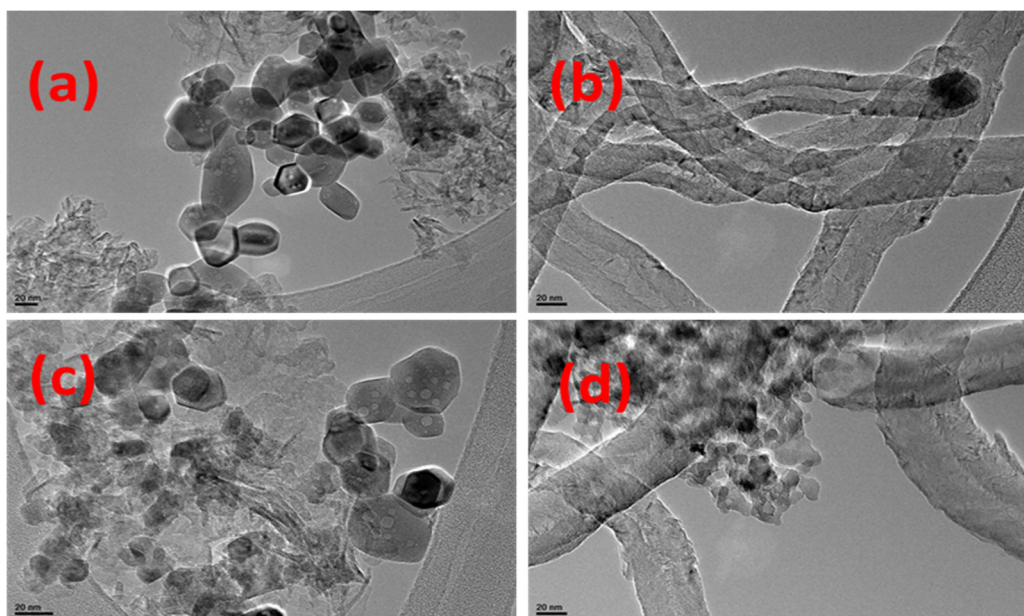


Figure 5. HR-TEM images of (a) 5Ni/SAPO-5, (b) 5Ni +1Sr/SAPO-5, (c) 5Ni +1Ce/SAPO-5, (d) 5Ni +1Cu/SAPO-5.

2.6. Temperature-Programmed Desorption (NH_3 -TPD)

Figure 6 depicts the NH_3 -TPD profiles of 5Ni/SAPO-5, 5Ni+1Sr/SAPO-5, 5Ni+1Ce/SAPO-5, and 5Ni+1Cu/SAPO-5. This study explored the acidity of 5Ni/SAPO-5 with (1Sr/1Ce/1Cu) and 5Ni/SAPO-5 solitary catalysts using the NH_3 temperature programmed desorption approach (NH_3 -TPD). Table 1 articulates the acidity levels of the catalysts as ascertained by the temperature-programmed desorption approach. There were significantly more acid sites observed on the 5Ni+1Sr/SAPO-5 catalyst (1.65 mmol/g) than on the 5Ni/SAPO-5 catalyst (1.03 mmol/g). It shows that a broad range of acid strengths were exhibited by all of the catalysts that were generated [44]. It was observed that the catalysts 5Ni+1Ce/SAPO-5 and 5Ni+1Cu/SAPO-5 only showed a single peak at about 300 °C, but the supported catalysts, 5Ni +1Sr/SAPO-5, had two peaks at 300 °C and 480 °C [45,46]. The low-temperature peak is commonly attributed to NH_3 adsorbed on weak acid sites; however, the peak at 400 to 500 °C has been connected to NH_3 adsorbed on strong acid sites. Based on the peak position of the desorbed ammonia with temperature, the acidic sites were categorized as low (below 200 °C), moderate (200 to 350 °C), and strong (>350 °C). The range of 150 to 500 °C showed NH_3 desorption peaks in all of the produced catalysts. The 5Ni/SAPO-5

distribution may widen as a result of the species concentration in SAPO-5. The maximum number of detected acid sites on the 5Ni+1Sr/SAPO-5 catalysts, as shown in (Figure 6), indicates that the generated catalysts typically have significantly higher acid site densities. Here is the order in which the samples' acidity increases: 5Ni/SAPO-5 < 5 Ni+1Ce/SAPO-5 < 5 Ni+1Sr/SAPO-5 < 5 Ni+1Cu/SAPO-5.

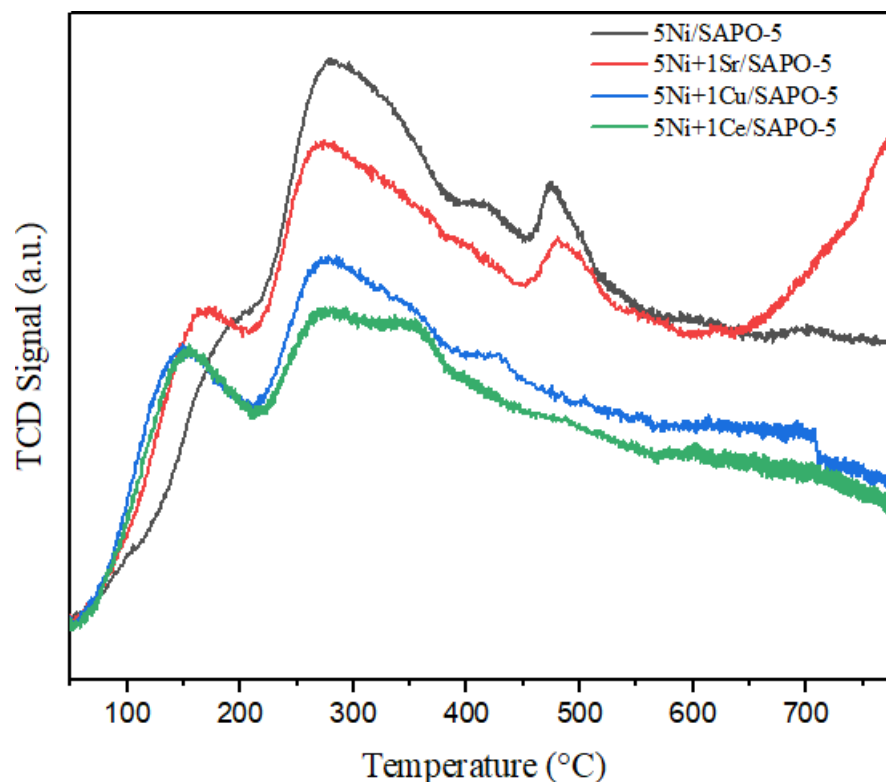


Figure 6. NH₃-TPD Profile images of 5Ni/SAPO-5 and 5Ni +1x/SAPO-5 (x = Sr, Cu, and Ce).

2.7. Raman Spectra Pure Catalyst

Figure 7 presents the Raman spectra of Ni supported on SAPO-5 samples containing Sr, Cu, and Ce promoters, compared to pure Ni with SAPO-5. By identifying the metal-oxide vibrational modes in each of these synthesized catalysts, Raman spectroscopy was used to acquire insight into the supported SAPO-5 structures generated in each of the various samples (Figure 7). The Ni–O stretching mode is responsible for the broad and intense band that is visible in the pure Ni Raman spectra between 500 cm⁻¹ and 1000 cm⁻¹. Furthermore, it was mentioned that the ring configurations that make up the molecular sieve lattice are known to be highly sensitive to Raman spectroscopy. Specifically, signals at 270 and 500 cm⁻¹ are linked to 10R and 4R rings for AlPO₄-n and SAPO-n molecular sieves. According to the Raman spectra, the stretching and bending vibrations of the molecular sieve framework are responsible for the strong bands located at 1121 and 498 cm⁻¹, respectively, Si–O–Si ν (450–550 cm⁻¹). Additionally, it was claimed that the one-phonon (1P) longitudinal optical (LO) and transverse optical (TO) of Ni vibrational modes correlate to the Raman peaks at 400 and 530 cm⁻¹, respectively. The two-phonon 2PTO, 2PTO+LO, and 2PLO of the Ni vibrational modes are represented by the peaks at 1090 cm⁻¹, respectively. The disorder caused by irregularities and surface imperfections is responsible for the existence of the LO mode. Furthermore, 5Ni/1Sr supported on SAPO-5 exhibited a low intense peak at 2200 cm⁻¹ and 5Ni/1Ce and 5Ni/1Cu supported with SAPO-5 showed two shoulder peaks, which correspond to the low concentration of the bimetallic species [47,48]. Figure 1 also exhibits the Raman spectrum of the SAPO-5 calcined catalyst support.

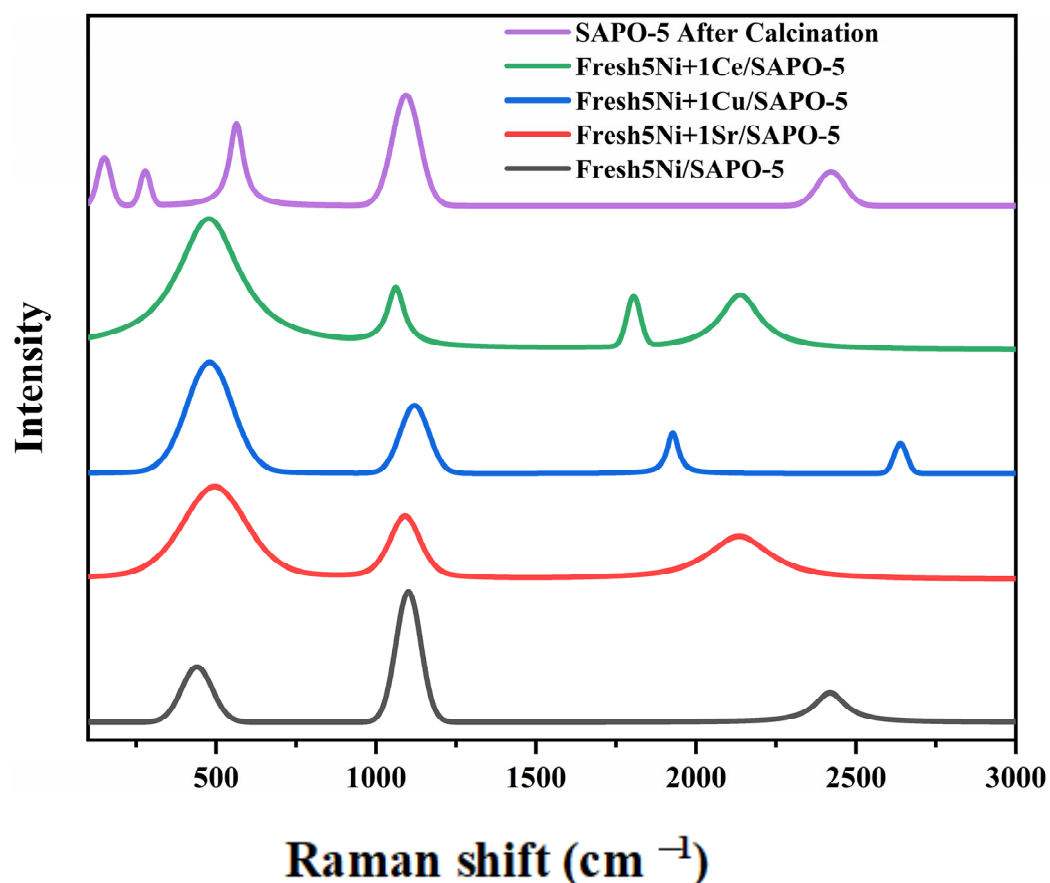


Figure 7. Raman spectra pure catalysts of 5Ni/SAPO-5 and 5Ni +1x/SAPO-5 (x = Sr, Cu, and Ce).

3. Catalytic Activity of Partial Oxidation of Methane to Hydrogen

To enhance syngas production through faster reaction rates, POMs require catalysts. According to Wang et al.'s [49] thermodynamic calculations, operating at 600 °C and atmospheric pressure yields the maximum achievable equilibrium conversion, product yield, and H₂:CO ratio. According to Siang et al. [50], before entering the catalyst bed, CH₄ combustion along with direct methane partial oxidation procedures took place in the hotter regions. After getting into the catalyst bed, the predominant reactions transform towards CH₄ combustion. As evidenced by the data, the significance of the passive combustion-reforming pathway was proven by the intermediate H₂O and CO₂ developed during the combustion of CH₄. Furthermore, carbon deposits would inevitably form, but they might be gradually repressed as high temperatures and rising CH₄/O₂ ratios would cause them to do so.

In this scientific study, the performance of the synthetic catalysts was assessed together with their synthesized counterparts for comparison. POM assays were performed on all of the prepared catalysts, such as 5Ni/SAPO-5, 5Ni+1Sr/SAPO-5, 5Ni+1Cu/SAPO-5, and 5Ni+1Ce/SAPO-5. Additionally, to ensure consistency in the results, all of the synthesized catalysts in the reactor with a 0.1 g loading were tested for 8.5 h (TOS) following the induction period at 600 °C and CH₄/O₂ = 2. Each of the presented values in Figures 8–11 is an average value obtained after the induction time, and it compares the CH₄ conversion, H₂/CO ratio, and yield of H₂, CO, and CO₂ for all the produced catalysts.

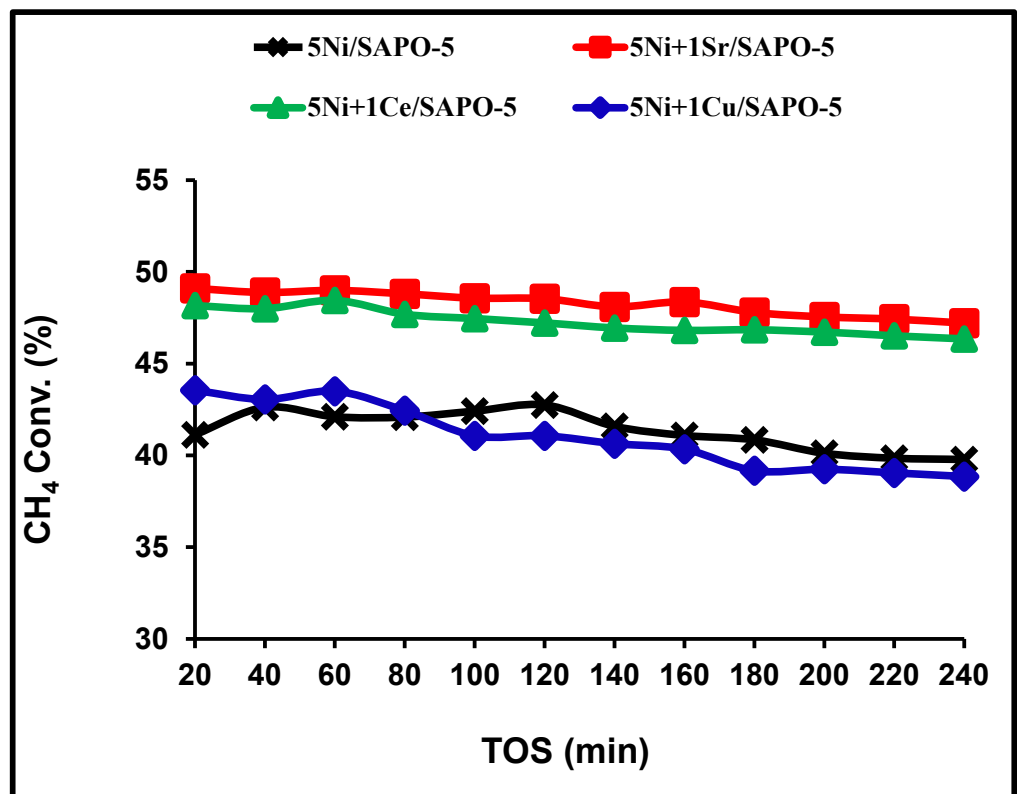


Figure 8. CH₄ Conversions of 5Ni/SAPO-5 and 5Ni +1x/SAPO-5 (x = Sr, Cu, and Ce).

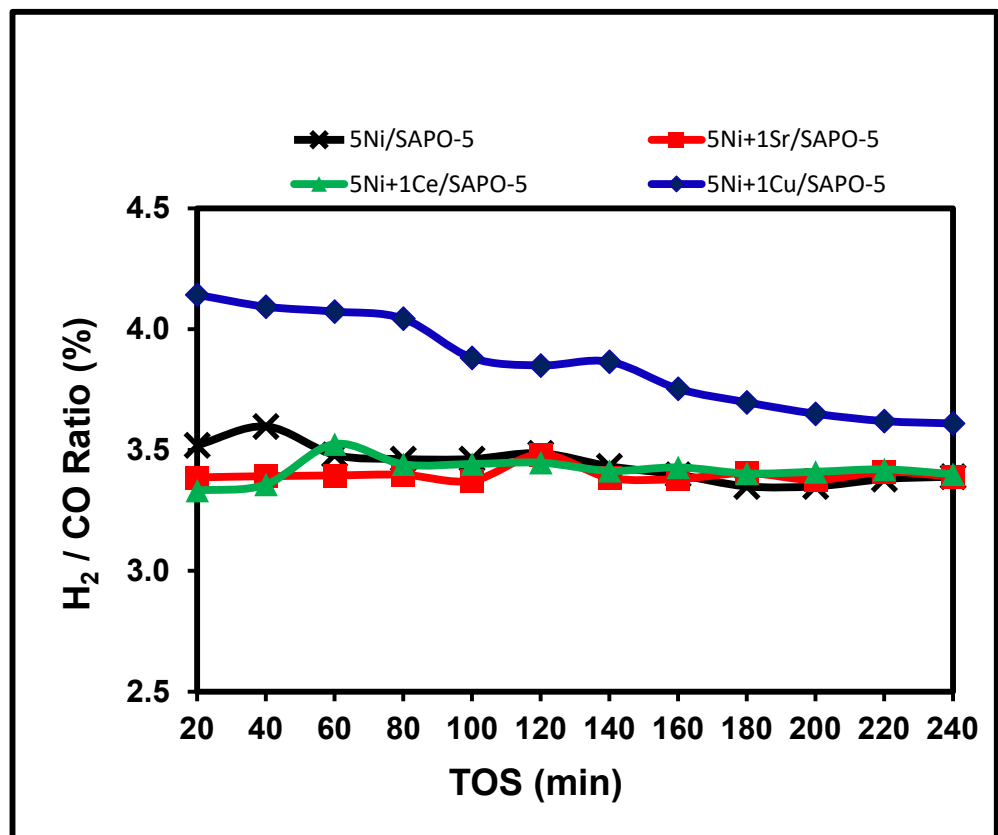


Figure 9. H₂/CO Ratios of 5Ni/SAPO-5 and 5Ni +1x/SAPO-5 (x = Sr, Cu, and Ce).

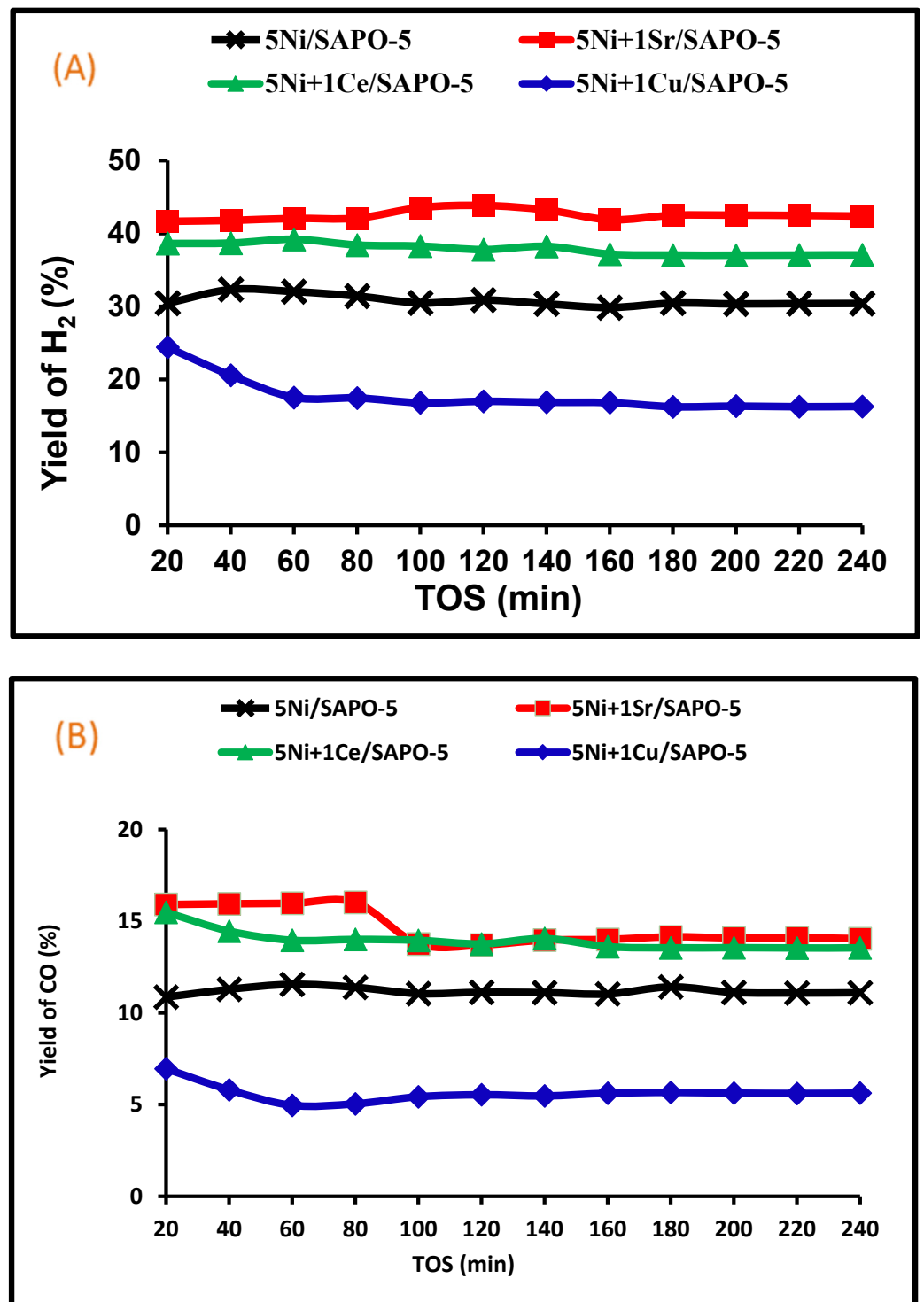


Figure 10. (A,B) Yield of Syngas by H₂ and CO of 5Ni/SAPO-5 and 5Ni +1x/SAPO-5 (x = Sr, Cu, and Ce).

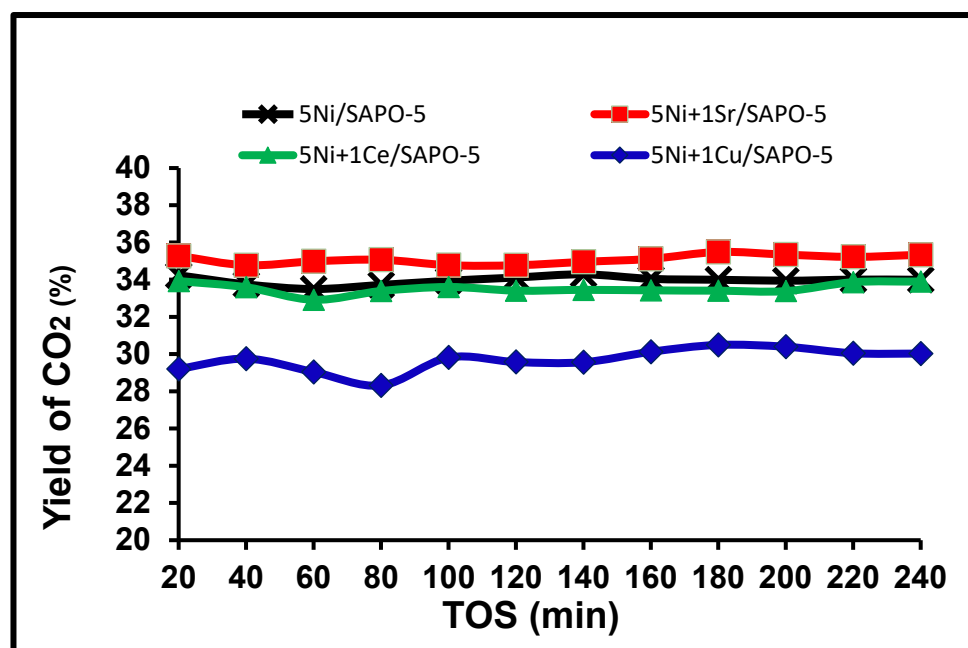


Figure 11. Yield of CO₂ by 5Ni/SAPO-5 and 5Ni +1x/SAPO-5 (x = Sr, Cu, and Ce).

3.1. CH₄ Conversion

The rate of CH₄ conversion of synthesized Ni supported on SAPO-5 with Sr, Ce, and Cu promoters is exhibited in Figure 8. The findings demonstrate that adding Sr, Ce, and Cu promoters and Ni to SAPO-5 significantly improves both syngas selectivity and CH₄ conversion. In contrast, 5Ni/SAPO-5 only exhibits 41.13% CH₄ conversion; this lower catalytic behavior is attributed to its semi-crystalline structure at high temperatures. Agglomeration caused low active areas for chemical reactions to emerge on the surface as a result. Nevertheless, the CH₄ conversion value rose from 41.13% to 43.55% when Cu was added to the 5Ni/SAPO-5. Additionally, the addition of Ce and Sr as active promoters to the catalyst resulted in higher CH₄ conversion values for 5Ni+1Ce/SAPO-5 and 5Ni+1Sr/SAPO-5, respectively, at 48.17% and 49.11%, owing to the significant affinity of Ni, Ce, and Sr for breaking the C–H bonds of CH₄. Furthermore, the presence of numerous oxides in SAPO-5, including SiO₂, P₂O₅, and Al₂O₃, offers the advantage of multi-metallic support in addition to enhancing catalytic activity. This may be related to the assembly of a cubical structure similar to NiAl₂O₄, as revealed by XRD [29]. This mechanism is further supported by the assertion that Ni and promoter loading on the SAPO-5 catalyst surface enhances the proportion of active metallic sites (Ni⁰) and oxygen centers in an attempt to boost catalytic activity. Based on the fact that Sr (s-block—[Kr] 5s²) occupies its valence electrons in the d orbital (electronic configuration), Ni (d-block—[Ar] 3d⁸, 4s²), Cu (d-block ([Ar] 3d¹⁰, 4s¹), and Ce (f-block—[Xe] 4f¹ 5d³ 6s²) are transition metals. The two unpaired electrons in the d orbital are accessible and can bond with a gaseous reactant (CH₄) with ease, by Hund's rule. Furthermore, the interaction between the promoter and active metal (Ni), which provides new and more Ni-active centers for CH₄ conversion, can also be credited with the improvement in catalyst performance [28]. Overall, considering the CH₄ conversion, the catalytic outcomes for Ni+1Sr/SAPO-5 are favorable.

3.2. H₂/CO Ratio

The 5Ni/SAPO-5, 5Ni+1Sr/SAPO-5, 5Ni+1Cu/SAPO-5, and 5Ni+1Ce/SAPO-5 samples undergo a stability test, which is carried out for 240 min on TOS, as illustrated in Figure 9. The H₂/CO ratio of the synthesized catalysts is displayed for 8.5 h (TOS). The highest H₂/CO ratio of approximately 4.14 was seen in 5Ni+1Cu/SAPO-5, while the lowest ratio of 3.33 was found in 5Ni+1Ce/SAPO-5.

Consequently, based on the justification given above, it can be said that SAPO-5's multiple oxide composition offers the advantages of a multimetallic support system, increasing POM activity and fostering a strong bond between the active metal and platform. The catalyst's solid-state reaction or the activation of Ni particles may have contributed to the initial few-hour increase in catalytic activity. The catalytic activity stabilized on the stream after a few hours, with an approximate H₂/CO ratio of 3.40. Positive signs for the final catalyst include the Ni+1Sr/SAPO-5 catalyst's outstanding stability and catalytic activity for 30 h on TOS without deactivation. Owing to the development of mixed metal oxides on the catalyst surface, the catalyst exhibits remarkable catalytic activity and resistance to deactivation. Therefore, it renders the SAPO-5 a viable substitute for existing commercially accessible supports, although its high cost continues to pose a significant challenge [51,52].

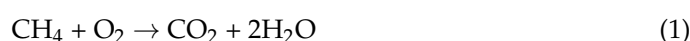
3.3. Yield of Syngas

The generation of CO and hydrogen (Syngas) over the investigated catalytic materials is shown in Figure 10A,B. The methane breakdown and CO disproportionation can account for the minor drop in hydrogen and CO yield for some catalysts shown in Figure 10 as a function of time-on-stream. The addition of 5Ni+1Cu/SAPO-5 appears to reduce the catalyst's stability at the initial phase of the experiment, according to Figure 11. Nonetheless, the stability (H₂ production) does not change after 80 min of TOS. At the inception of the experiment, 5Ni/SAPO-5 slightly increased activity, and the catalyst was equally stable as 5Ni+1Ce/SAPO-5.

When assessing stability based on syngas generation, 5Ni+1Sr/SAPO-5 alone appears to be fairly stable. When comparing 5Ni+1Sr/SAPO-5 to 5Ni+1Ce/SAPO-5, both product yields were higher, regardless of TOS. The initial yield of CO for 5Ni+1Sr/SAPO-5 was 15.91%, while the initial yield of H₂ was around 41.66%. The H₂ and CO yields for the Sr-supported catalyst, which were observed at roughly 43.56% and 13.76%, respectively, at steady-state conditions, were significantly greater than those of the non-supported catalyst. Although the CO production of the Sr-based catalyst showed a drop in stability, the H₂ yield remained quite substantial throughout. It was predicted that the 5Ni+1Sr/SAPO-5-promoted catalysts would provide syngas yields far greater than the transition-promoted samples.

3.4. Yield of CO₂

The impact of CO₂ produced during the partial oxidation of methane is depicted in Figure 11. In contrast to the other catalysts (5Ni/SAPO-5, 5Ni+1Ce+SAPO-5, and 5Ni+1Cu/SAPO-5), 5Ni+1Sr+SAPO-5 demonstrated a greater yield (35.28%) of CO₂ and retained its catalytic stability for 240 min, as apparent in Figure 11. Methane undergoes partial oxidation through two reversible and one nonreversible process, both of which have been documented in the literature [53]. Methane oxidation results in an immense amount of carbon oxide emission. Syngas is only partially formed and has a low reaction selectivity to carbon monoxide; this is caused by steam and carbon dioxide reforming. Maximum hydrogen generation occurs at a methane conversion of 40–60%, depending on reaction temperature. At that point, the equilibrium of processes (2) and (3) significantly shifts in favor of the reactants, lowering the reactor's concentration of hydrogen and carbon monoxide. Recycling the carbon dioxide from the combustion reaction that is not converted to syngas back into the reactor feed can increase syngas production by directing carbon dioxide reforming in the direction of syngas production. Increased carbon dioxide levels in the reactor contribute to a decrease in the H₂/CO ratio and an increase in the amount of syngas earned.



3.5. Activity of 5Ni+1Sr/SAPO-5 at Different Reaction Temperatures

The impact of process temperature on the conversion and selectivity of methane to hydrogen is expressed graphically in Figure 12A,B. The analysis has been conducted using their optimal metal catalyst, 5Ni+1Sr/SAPO-5. The catalytic activity variability of 5Ni+1Sr/SAPO-5 across 600 and 750 °C can be witnessed in the conversion and selectivity exploration laid out in Figure 12A,B. According to the CH₄ conversion study, the conversion percentage ranges from 49.11 to 82.67%, as indicated in Figure 12A. Under 750 °C, the CH₄ conversion rate persisted at 78.47% for 240 min of TOS. The yield of hydrogen during the conversion of CH₄ is highlighted in Figure 12B. Once more, the 600–750 °C temperature range was the focus of the analysis. Even at a higher temperature of 750 °C, the most significant yield of 72.67% was achieved. In the case of 240 min of TOS at 750 °C, the catalyst's activity claimed its lowest achievable stability of 69.35%. Figure S1 of the support information shows the hydrogen yield (%) versus time-on-stream (TOS) at various reaction temperatures.

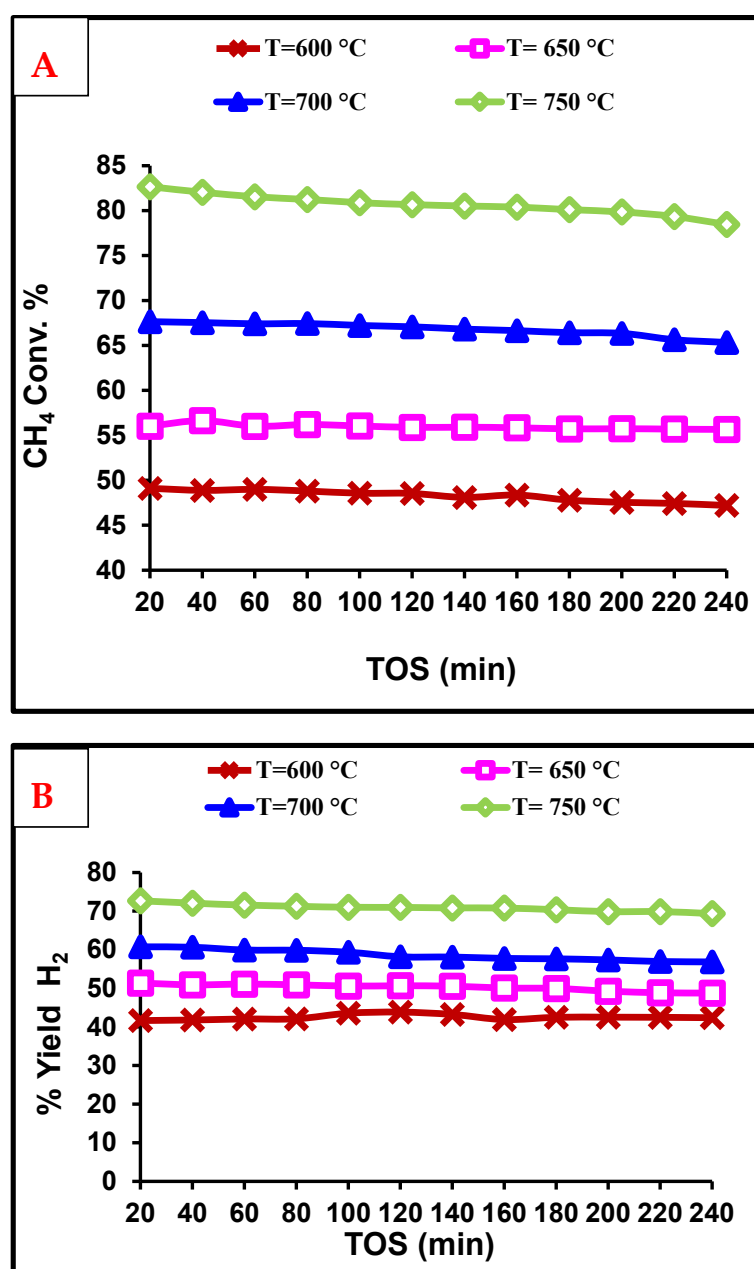


Figure 12. The catalytic activity of 5Ni+1Sr/SAPO-5: (A) CH₄ conversion; (B) CO₂ conversion at different reaction temperatures.

3.6. Raman Spectra for Used Catalyst

Raman spectroscopy was used to characterize the carbon deposits on the catalysts used (spectra are displayed in Figure 13). To ensure uniformity of the composition, Raman spectra were acquired for each sample at several locations. The carbon Raman spectra indicated two distinct modes, denoted as G (graphitic) and D (disordered), respectively, at approximately 1590 and 1350 cm^{-1} . These modes are associated with the production of amorphous carbon or imperfect carbon filaments. The I_D/I_G ratio, also known as the D band to G band intensity ratio, is a crucial parameter obtained from Raman spectroscopy that provides information about the structural disorder and defects in carbon-based materials, particularly graphene and carbon nanotubes. The D band corresponds to the disorder-induced peak, while the G band represents the first-order scattering from sp^2 carbon atoms. A higher I_D/I_G ratio indicates a higher level of structural disorder and defects, while a lower ratio indicates fewer defects and a more ordered structure. Based on this, strontium-loaded 5Ni/SAPO-5 possesses I_D/I_G of 1.3, indicating a higher level of disorders, which is correspondingly reflected in its conversion and selectivity for partial oxidation of methane. A feature of carbon nanotubes, the splitting of the G band results in the presentation of an extra band approximately 1570 cm^{-1} in this used catalyst [54].

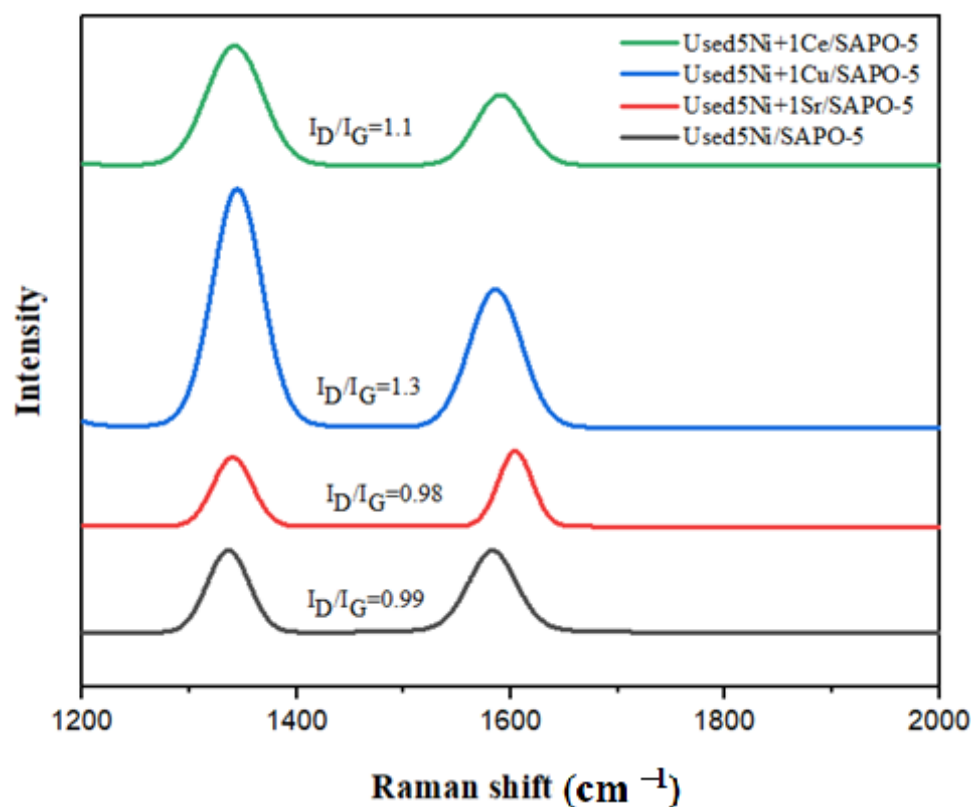


Figure 13. Raman spectra for used catalysts of 5Ni/SAPO-5 and 5Ni+1x/SAPO-5 (x = Sr, Cu, and Ce).

3.7. Reaction Mechanism for POM

The mechanism for H_2 and CO formation in catalytic partial oxidation is complex and not yet fully understood. Two possible mechanisms are direct partial oxidation (DPO) and indirect combustion and reforming reactions. Various factors, such as catalyst components, reaction conditions, and metal-support interaction, affect the reaction mechanisms [53,55]. In DPO, CH_4 dissociation leads to the formation of methyl radicals, H^* and C^* species, which are converted into syngas. In indirect combustion and reforming, CO_2 and H_2O are the primary products that may undergo steam or dry reforming and finally convert into syngas [56,57]. Solid base catalysts in POM heterogeneous catalysis are typically identified by the presence of basic groups on their surface. The catalysts were activated for one hour

in the presence of H₂, during which SrO and Ni₂ interacted in a reduced atmosphere by donating their electron pairs, which led to the formation of Sr²⁺ and Ni²⁺ ions [18,58]. These positive ions, or active sites, are responsible for CH₄ adsorption and H₂ formation via different routes. Uncovered O atoms are responsible for H⁺ abstraction from CH₄, forming OH⁻ ions, which are converted into water and lattice oxygen via OH⁻ coupling [59]. The conversion of SrO into its ions involves Sr²⁺ acting as Lewis acid and O²⁻ acting as Bronsted base. The electrophilicity of Sr²⁺ cation is due to its electronegativity, making its conjugated base (O²⁻) highly basic. Increasing the basic nature of a catalyst by adding active sites and lattice oxygen enhances catalytic performance. Ni and Sr interactions result in the formation of H₂ molecules. Syngas can be synthesized directly by combining adsorbed C and H₂O. Increased oxygen consumption exposes more active sites to CH₄ adsorption and generates more H₂. However, CO can oxidize into CO₂, but it can easily dissociate again into CO. It has also been explained in the literature that low energy barriers are required for CO₂ dissociation into CO [60]. As a result of increased oxygen consumption, more active sites are exposed to CH₄ adsorption and increased H₂ generation, as shown in Figure 14. The following Equations (4)–(14) show the partial oxidation of CH₄ to syngas over a Ni-Sr/SAPO-5 catalyst:

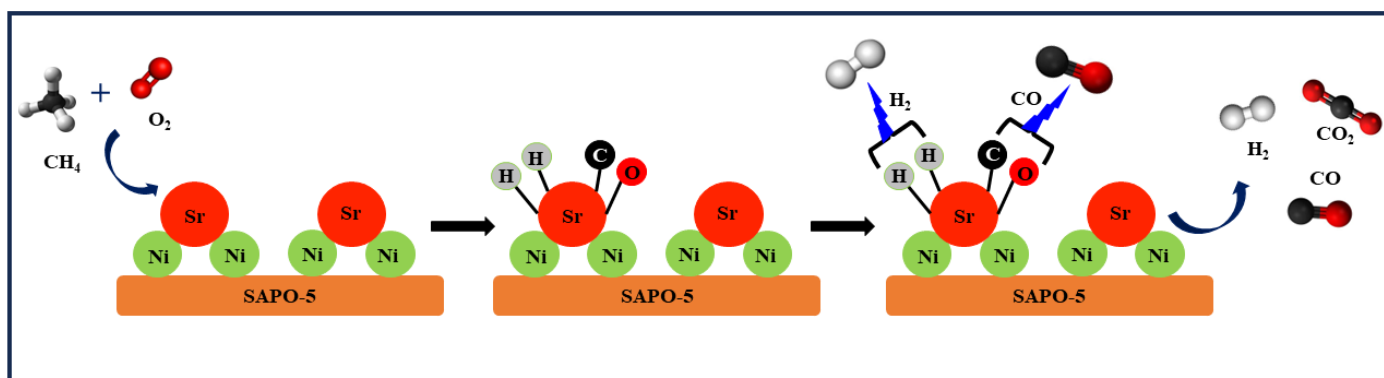
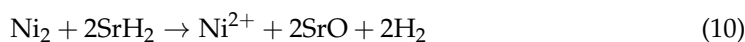
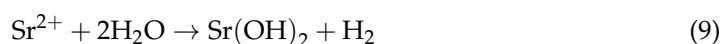


Figure 14. Partial oxidation of CH₄ to syngas over Ni-Sr/SAPO-5 catalyst.

4. Materials and Methods

4.1. Catalyst Preparation

A 5 wt.% equivalent of Ni(NO₃)₂·6H₂O aqueous solution and a promoters' nitrate solution containing cerium, copper, and strontium (1 wt.%) is wet-impregnated onto a SAPO-5 support while stirring at 85 °C. Stirring continues until a solution evaporates and

the mixture turns into a paste. The solution was dried at 120 °C for 24 h and then calcined at 600 °C for 3 h. The catalyst is abbreviated as 5Ni/SAPO-5 and Ni+1x/SAPO-5 (x = Ce, Cu, and Sr).

4.2. Catalyst Characterization

Powder X-ray diffraction (XRD) analysis of fresh catalyst was conducted by a Rigaku (Miniflex, Tokyo, Japan) diffractometer using Cu K α 1 radiation ($\lambda = 0.15406$ nm) operated at 40 mA and 40 kV. The N₂ adsorption-desorption and porosity results were obtained using a Micromeritics Tristar II 3020 surface area analyzer (Micromeritics, Norcross, GA, USA). An amount of 0.2–0.3 g of catalyst was degassed, and all samples were degassed before analysis using the Barrett, Joyner, and Halenda (BJH) method. Temperature-programmed hydrogen reduction (H₂-TPR) and temperature-programmed desorption (NH₃-TPD) measurements were performed on a chemisorption device (Micromeritics Auto Chem II) by using a thermal conductivity detector over a 70 mg catalyst sample, respectively. In H₂-TPR, H₂ absorption is monitored up to 1000 °C under 10% H₂/He gas, whereas in NH₃-TPD, NH₃ desorption is monitored upon raising the temperature to 800 °C under 10% NH₃/He gas. The transmission electron microscopy was conducted at 200 kV using an aberration-corrected JEM-ARM200F (JEOL, Tokyo, Japan) with a CEOS corrector (CEOS GmbH, Heidelberg, Germany). The spent catalyst sample underwent Raman analysis within the 1250–3000 cm⁻¹ range using a laser Raman spectrometer (JASCO, Tokyo, Japan) with a 532 nm beam excitation and 1.6 mW laser intensity. The exposure time was set to 10 s with 3 accumulations. The spectra were processed using Spectra Manager Ver.2 software (JASCO, Japan).

4.3. Catalyst Activity Test

An amount of 0.1 g of catalyst sample was packed in a tubular stainless steel fixed-bed reactor (PID Eng & Tech, Madrid, Spain, 9 mm I.D.). The reactor's temperature is monitored by a K-type thermocouple fitted axially at the center of the catalyst bed. Before the reaction, the catalyst was reduced by flowing hydrogen at a 30 mL/min flow rate for 1 h at 600 °C. Following the impregnation, the reactor is flushed with nitrogen gas (N₂) to eliminate any residual hydrogen gas (H₂) present in the system. Then the temperature of the reactor is stabilized at 600 °C. The packed catalyst is exposed to a mixture of CH₄ and O₂ gases in a 2:1 ratio. The volume ratio of feed gases (CH₄/O₂) was set to 2. Furthermore, the space velocity was maintained at 14,400 mL/h/gcat, and the feed rates for CH₄, O₂, and N₂ were 12, 6, and 6, with a total feed rate of 24 mL/min. The product is analyzed by a gas chromatograph equipped with a propak Q column, molecular sieve columns, and a thermal conductivity detector. The composition of effluent gases was calculated by the normalization method, and the equations for the determination of CH₄ conversion, H₂ yield, and H₂/CO ratio are used as follows:

$$\text{CH}_4 \text{ conversion} = \frac{\text{CH}_{4,\text{in}} - \text{CH}_{4,\text{out}}}{\text{CH}_{4,\text{in}}} \times 100\% \quad (15)$$

$$\text{H}_2 \text{ Yield (\%)} = \frac{\text{H}_{2,\text{out}}}{2 \times \text{CH}_{4,\text{in}}} \times 100 \quad (16)$$

$$\frac{\text{H}_2}{\text{CO}} = \frac{\text{Mole of H}_2 \text{ produced}}{\text{Mole of CO produced}} \quad (17)$$

5. Conclusions

Effective implementation and investigation of the catalytic activity of 5Ni/SAPO-5, 5Ni+1Sr/SAPO-5, 5Ni+1Ce/SAPO-5, and 5Ni+1Cu/SAPO-5 catalysts produced via wetness impregnation were performed for POM. Based on its characterization aspects, the catalyst was found to possess the required physicochemical properties, such as a crystalline structure and strong thermal stability up to 850 °C. Ni was used as the active metal over SAPO-5, which increased the catalytic performance. 5Ni+1Sr/SAPO-5 exhibited improved

stability and performance for 240 min at 600 °C, with a CH₄ conversion of 48.17% and an H₂/CO ratio of 3.33 without deactivation. The catalyst's stability implies the efficient and cost-effective usage of the synthesized bimetallic SAPO-5-supported catalyst for the production of hydrogen-rich syngas and other possible catalytic applications.

Supplementary Materials: The following supporting information can be downloaded at: <https://www.mdpi.com/article/10.3390/catal14050316/s1>, Figure S1: Hydrogen Yield (%) versus Time-On-Stream (TOS) at Various Reaction Temperatures; Table S1: H₂ Uptake During TPR Analysis calcined at 600 °C 5.

Author Contributions: A.A.-A. and A.S.A.-F.: methodology, conceptualization, investigation, data curation, writing—review and editing; A.H.F., A.E.A. and A.A.I.: methodology, formal analysis, supervision; J.A.-D.: formal analysis, Funding acquisition, Validation, K.C., S.S. and O.B.: data curation writing—original draft preparation. All authors have read and agreed to the published version of the manuscript.

Funding: Researchers Supporting Project number (RSP2024R368), King Saud University.

Data Availability Statement: Data are contained within the article and Supplementary Materials.

Acknowledgments: The authors would like to extend their sincere appreciation to the Researchers Supporting Project number (RSP2024R368), King Saud University, Riyadh, Saudi Arabia. JAD acknowledges Queen's University Belfast for supporting research.

Conflicts of Interest: The authors declare no conflict of interest.

References

1. Wang, Y.; Kang, Y.; Ge, M.; Zhang, X.; Zhan, L. Cerium and Tin Oxides Anchored onto Reduced Graphene Oxide for Selective Catalytic Reduction of NO with NH₃ at Low Temperatures. *RSC Adv.* **2018**, *8*, 36383–36391. [CrossRef]
2. Metin, D.; Tihminlioglu, F.; Balköse, D.; Ülkü, S. The Effect of Interfacial Interactions on the Mechanical Properties of Polypropylene/Natural Zeolite Composites. *Compos. Part A Appl. Sci. Manuf.* **2004**, *35*, 23–32. [CrossRef]
3. Javed, A.H.; Shahzad, N.; Butt, F.A.; Khan, M.A.; Naeem, N.; Liaquat, R.; Khoja, A.H. Synthesis of Bimetallic Co-Ni/ZnO Nanoprisms (ZnO-NPr) for Hydrogen-Rich Syngas Production via Partial Oxidation of Methane. *J. Environ. Chem. Eng.* **2021**, *9*, 106887. [CrossRef]
4. Junke, X.U.; Wei, Z.; Jihui, W.; Zhaojing, L.I.; Jianxin, M.A. Characterization and Analysis of Carbon Deposited during the Dry Reforming of Methane over Ni/La₂O₃/Al₂O₃ Catalysts. *Chin. J. Catal.* **2009**, *30*, 1076–1084.
5. Schnabel, K.-H.; Finger, G.; Kornatowski, J.; Löffler, E.; Peuker, C.; Pilz, W. Decomposition of Template in SAPO-5 and AlPO₄-5 Molecular Sieves Studied by IR and Raman Spectroscopy. *Microporous Mater.* **1997**, *11*, 293–302. [CrossRef]
6. Danilina, N.; Castelanelli, S.A.; Troussard, E.; van Bokhoven, J.A. Influence of Synthesis Parameters on the Catalytic Activity of Hierarchical SAPO-5 in Space-Demanding Alkylation Reactions. *Catal. Today* **2011**, *168*, 80–85. [CrossRef]
7. Sharma, P.; Sebastian, J.; Ghosh, S.; Creaser, D.; Olsson, L. Recent Advances in Hydrogenation of CO₂ into Hydrocarbons via Methanol Intermediate over Heterogeneous Catalysts. *Catal. Sci. Technol.* **2021**, *11*, 1665–1697. [CrossRef]
8. Kim, H.W.; Kang, K.M.; Kwak, H.-Y. Preparation of Supported Ni Catalysts with a Core/Shell Structure and Their Catalytic Tests of Partial Oxidation of Methane. *Int. J. Hydrogen Energy* **2009**, *34*, 3351–3359. [CrossRef]
9. Ma, Q.; Guo, L.; Fang, Y.; Li, H.; Zhang, J.; Zhao, T.-S.; Yang, G.; Yoneyama, Y.; Tsubaki, N. Combined Methane Dry Reforming and Methane Partial Oxidization for Syngas Production over High Dispersion Ni Based Mesoporous Catalyst. *Fuel Process. Technol.* **2019**, *188*, 98–104. [CrossRef]
10. Jin, R.; Chen, Y.; Li, W.; Cui, W.; Ji, Y.; Yu, C.; Jiang, Y. Mechanism for Catalytic Partial Oxidation of Methane to Syngas over a Ni/Al₂O₃ Catalyst. *Appl. Catal. A Gen.* **2000**, *201*, 71–80. [CrossRef]
11. Pompeo, F.; Nichio, N.N.; Ferretti, O.A.; Resasco, D. Study of Ni Catalysts on Different Supports to Obtain Synthesis Gas. *Int. J. Hydrogen Energy* **2005**, *30*, 1399–1405. [CrossRef]
12. Guo, S.; Wang, J.; Ding, C.; Duan, Q.; Ma, Q.; Zhang, K.; Liu, P. Confining Ni Nanoparticles in Honeycomb-like Silica for Coking and Sintering Resistant Partial Oxidation of Methane. *Int. J. Hydrogen Energy* **2018**, *43*, 6603–6613. [CrossRef]
13. Védrine, J.C. Heterogeneous Catalysis on Metal Oxides. *Catalysts* **2017**, *7*, 341. [CrossRef]
14. Fleys, M.; Simon, Y.; Swierczynski, D.; Kiennemann, A.; Marquaire, P.-M. Investigation of the Reaction of Partial Oxidation of Methane over Ni/La₂O₃ Catalyst. *Energy Fuels* **2006**, *20*, 2321–2329. [CrossRef]
15. Enger, B.C.; Lødeng, R.; Holmen, A. A Review of Catalytic Partial Oxidation of Methane to Synthesis Gas with Emphasis on Reaction Mechanisms over Transition Metal Catalysts. *Appl. Catal. A Gen.* **2008**, *346*, 1–27. [CrossRef]

16. Dedov, A.G.; Loktev, A.S.; Danilov, V.P.; Krasnobaeva, O.N.; Nosova, T.A.; Mukhin, I.E.; Baranchikov, A.E.; Yorov, K.E.; Bykov, M.A.; Moiseev, I.I. Catalytic Materials Based on Hydrotalcite-Like Aluminum, Magnesium, Nickel, and Cobalt Hydroxides: Effect of the Nickel/Cobalt Ratio on the Results of Partial Oxidation and Dry Reforming of Methane to Synthesis Gas. *Pet. Chem.* **2020**, *60*, 194–203. [\[CrossRef\]](#)
17. Raza, J.; Khoja, A.H.; Naqvi, S.R.; Mehran, M.T.; Shakir, S.; Liaquat, R.; Tahir, M.; Ali, G. Methane Decomposition for Hydrogen Production over Biomass Fly Ash-Based CeO₂ Nanowires Promoted Cobalt Catalyst. *J. Environ. Chem. Eng.* **2021**, *9*, 105816. [\[CrossRef\]](#)
18. Tavizón-Pozos, J.A.; Chavez-Esquivel, G.; Suárez-Toriello, V.A.; Santolalla-Vargas, C.E.; Luévano-Rivas, O.A.; Valdés-Martínez, O.U.; Talavera-López, A.; Rodríguez, J.A. State of Art of Alkaline Earth Metal Oxides Catalysts Used in the Transesterification of Oils for Biodiesel Production. *Energies* **2021**, *14*, 1031. [\[CrossRef\]](#)
19. Corma, A.; Iborra, S. Optimization of Alkaline Earth Metal Oxide and Hydroxide Catalysts for Base-Catalyzed Reactions. *Adv. Catal.* **2006**, *49*, 239–302.
20. Pauletto, G.; Mendil, M.; Libretto, N.; Mocellin, P.; Miller, J.T.; Patience, G.S. Short Contact Time CH₄ Partial Oxidation over Ni Based Catalyst at 1.5MPa. *Chem. Eng. J.* **2021**, *414*, 128831. [\[CrossRef\]](#)
21. Belviso, C. State-of-the-Art Applications of Fly Ash from Coal and Biomass: A Focus on Zeolite Synthesis Processes and Issues. *Prog. Energy Combust. Sci.* **2018**, *65*, 109–135. [\[CrossRef\]](#)
22. Grabchenko, M.; Pantaleo, G.; Puleo, F.; Vodyankina, O.; Liotta, L.F. Ni/La₂O₃ Catalysts for Dry Reforming of Methane: Effect of La₂O₃ Synthesis Conditions on the Structural Properties and Catalytic Performances. *Int. J. Hydrogen Energy* **2021**, *46*, 7939–7953. [\[CrossRef\]](#)
23. Dedov, A.G.; Loktev, A.S.; Komissarenko, D.A.; Mazo, G.N.; Shlyakhtin, O.A.; Parkhomenko, K.V.; Kiennemann, A.A.; Roger, A.-C.; Ishmurzin, A.V.; Moiseev, I.I. Partial Oxidation of Methane to Produce Syngas over a Neodymium–Calcium Cobaltate-Based Catalyst. *Appl. Catal. A Gen.* **2015**, *489*, 140–146. [\[CrossRef\]](#)
24. Duan, Q.; Wang, J.; Ding, C.; Ding, H.; Guo, S.; Jia, Y.; Liu, P.; Zhang, K. Partial Oxidation of Methane over Ni Based Catalyst Derived from Order Mesoporous LaNiO₃ Perovskite Prepared by Modified Nanocasting Method. *Fuel* **2017**, *193*, 112–118. [\[CrossRef\]](#)
25. Ma, Y.; Ma, Y.; Zhao, Z.; Hu, X.; Ye, Z.; Yao, J.; Buckley, C.E.; Dong, D. Comparison of Fibrous Catalysts and Monolithic Catalysts for Catalytic Methane Partial Oxidation. *Renew. Energy* **2019**, *138*, 1010–1017. [\[CrossRef\]](#)
26. Arai, H.; Yamada, T.; Eguchi, K.; Seiyama, T. Catalytic Combustion of Methane over Various Perovskite-Type Oxides. *Appl. Catal.* **1986**, *26*, 265–276. [\[CrossRef\]](#)
27. Ross, J.R.H.; Steel, M.C.F. Mechanism of the Steam Reforming of Methane over a Coprecipitated Nickel-Alumina Catalyst. *J. Chem. Soc. Faraday Trans. 1 Phys. Chem. Condens. Phases* **1973**, *69*, 10–21. [\[CrossRef\]](#)
28. Özdemir, H.; Öksüzömer, M.A.F.; Gürkaynak, M.A. Preparation and Characterization of Ni Based Catalysts for the Catalytic Partial Oxidation of Methane: Effect of Support Basicity on H₂/CO Ratio and Carbon Deposition. *Int. J. Hydrogen Energy* **2010**, *35*, 12147–12160. [\[CrossRef\]](#)
29. López-Fonseca, R.; Jiménez-González, C.; de Rivas, B.; Gutiérrez-Ortiz, J.I. Partial Oxidation of Methane to Syngas on Bulk NiAl₂O₄ Catalyst. Comparison with Alumina Supported Nickel, Platinum and Rhodium Catalysts. *Appl. Catal. A Gen.* **2012**, *437*, 53–62. [\[CrossRef\]](#)
30. Dong, W.-S.; Jun, K.-W.; Roh, H.-S.; Liu, Z.-W.; Park, S.-E. Comparative Study on Partial Oxidation of Methane over Ni/ZrO₂, Ni/CeO₂ and Ni/Ce–ZrO₂ Catalysts. *Catal. Lett.* **2002**, *78*, 215–222. [\[CrossRef\]](#)
31. Kogler, M.; Köck, E.-M.; Perfler, L.; Bielz, T.; Stöger-Pollach, M.; Hetaba, W.; Willinger, M.; Huang, X.; Schuster, M.; Klötzer, B. Methane Decomposition and Carbon Growth on Y₂O₃, Ytria-Stabilized Zirconia, and ZrO₂. *Chem. Mater.* **2014**, *26*, 1690–1701. [\[CrossRef\]](#) [\[PubMed\]](#)
32. Zhang, X.; Zhang, Q.; Tsubaki, N.; Tan, Y.; Han, Y. Influence of Zirconia Phase on the Performance of Ni/ZrO₂ for Carbon Dioxide Reforming of Methane. In *Advances in CO₂ Capture, Sequestration, and Conversion*; ACS Publications: Washington, DC, USA, 2015; pp. 135–153. ISBN 1947-5918.
33. Moral, A.; Reyero, I.; Llorca, J.; Bimbela, F.; Gandía, L.M. Partial Oxidation of Methane to Syngas Using Co/Mg and Co/Mg-Al Oxide Supported Catalysts. *Catal. Today* **2019**, *333*, 259–267. [\[CrossRef\]](#)
34. Nemitallah, M.A. Characteristics of Hydrogen Separation and Methane Steam Reforming in a Pd-Based Membrane Reactor of Shell and Tube Design. *Case Stud. Therm. Eng.* **2023**, *45*, 102939. [\[CrossRef\]](#)
35. Chen, C.; Zhou, J.; Geng, J.; Bao, R.; Wang, Z.; Xia, J.; Li, H. Perovskite LaNiO₃/TiO₂ Step-Scheme Heterojunction with Enhanced Photocatalytic Activity. *Appl. Surf. Sci.* **2020**, *503*, 144287. [\[CrossRef\]](#)
36. Ojeda-Niño, O.; Gallego, J.; Daza, C.E. Pr-Promoted Ni Exsolution from Ni–Mg–Al (O) as Catalysts for Syngas Production by Dry Reforming of Methane. *Results Eng.* **2023**, *17*, 100821. [\[CrossRef\]](#)
37. Khoja, A.H.; Tahir, M.; Saidina Amin, N.A. Evaluating the Performance of a Ni Catalyst Supported on La₂O₃-MgAl₂O₄ for Dry Reforming of Methane in a Packed Bed Dielectric Barrier Discharge Plasma Reactor. *Energy Fuels* **2019**, *33*, 11630–11647. [\[CrossRef\]](#)
38. Hassan, N.S.; Jalil, A.A.; Twu, L.Y.; Fatah, N.A.A.; Hambali, H.U.; Hussain, I.; Firmansyah, M.L. Hydroisomerization of N-Hexane over Metal Oxides-Loaded Fibrous Silica Catalyst for Cleaner Fuel Production. *Int. J. Hydrogen Energy* **2023**, *48*, 20525–20537. [\[CrossRef\]](#)

39. Ma, Y.; Li, Z.; Zhao, N.; Teng, Y. One-Pot Synthesis of Cu–Ce Co-Doped SAPO-5/34 Hybrid Crystal Structure Catalysts for NH₃-SCR Reaction with SO₂ Resistance. *J. Rare Earths* **2021**, *39*, 1217–1223. [[CrossRef](#)]
40. Woo, J.; Leistner, K.; Bernin, D.; Ahari, H.; Shost, M.; Zammit, M.; Olsson, L. Effect of Various Structure Directing Agents (SDAs) on Low-Temperature Deactivation of Cu/SAPO-34 during NH₃-SCR Reaction. *Catal. Sci. Technol.* **2018**, *8*, 3090–3106. [[CrossRef](#)]
41. Yang, Y.; Liu, X.; Lyu, Y.; Liu, Y.; Zhan, W.; Yu, Z.; Fan, L.; Yan, Z. Enhanced Dispersion of Nickel Nanoparticles on SAPO-5 for Boosting Hydroisomerization of n-Hexane. *J. Colloid Interface Sci.* **2021**, *604*, 727–736. [[CrossRef](#)]
42. Sedighi, M.; Mohammadi, M.; Sedighi, M. Green SAPO-5 Supported NiO Nanoparticles as a Novel Adsorbent for Removal of Petroleum Asphaltenes: Financial Assessment. *J. Pet. Sci. Eng.* **2018**, *171*, 1433–1442. [[CrossRef](#)]
43. Dang, T.T.H.; Zubowa, H.L.; Benstrup, U.; Richter, M.; Martin, A. Microwave-Assisted Synthesis and Characterization of Cu-Containing AlPO₄-5 and SAPO-5. *Microporous Mesoporous Mater.* **2009**, *123*, 209–220. [[CrossRef](#)]
44. Alam, S.F.; Kim, M.-Z.; Rehman, A.U.; Arepalli, D.; Sharma, P.; Cho, C.H. Synthesis of SAPO-34 Nanoplates with High Si/Al Ratio and Improved Acid Site Density. *Nanomaterials* **2021**, *11*, 3198. [[CrossRef](#)] [[PubMed](#)]
45. Chuseang, J.; Itthibenchapong, V.; Srifa, A.; Praikaew, W.; Tuntithavornwat, S.; Rungtaweivoranit, B.; Ratchahat, S.; Koo-Amornpattana, W.; Klysubun, W.; Eiad-ua, A. Enhancing the Hydrodeoxygenation and Isomerization Using Re Nanoparticles Decorated on Ni/SAPO-11 Catalysts for Direct Production of Low-Cold Flow Diesel from Triglycerides. *ChemCatChem* **2023**, *15*, e202300543. [[CrossRef](#)]
46. Li, R.; Li, Z.; Chen, L.; Dong, Y.; Ma, S.; Yuan, F.; Zhu, Y. Synthesis of MnNi–SAPO-34 by a One-Pot Hydrothermal Method and Its Excellent Performance for the Selective Catalytic Reduction of NO by NH₃. *Catal. Sci. Technol.* **2017**, *7*, 4984–4995. [[CrossRef](#)]
47. Chen, Z.; Zhu, S.; Li, P.; Li, X.; Xu, Y.; Dong, Y.; Song, W.; Yi, X.; Fang, W. Fabricating Self-Assembled SAPO-5 with Tailored Mesoporosity and Acidity Using a Single Template. *CrystEngComm* **2017**, *19*, 5275–5284. [[CrossRef](#)]
48. Vorobyeva, E.E.; Shamanaeva, I.A.; Polukhin, A.V.; Lysikov, A.I.; Parkhomchuk, E. V SAPO-Containing Alumina CoMoNi-Catalysts for Hydrotreatment of Heavy Oil: Pore Hierarchy as a Key Parameter for Catalyst Stabilization. *Fuel* **2023**, *334*, 126676. [[CrossRef](#)]
49. Wang, Y.; Yao, L.; Wang, S.; Mao, D.; Hu, C. Low-Temperature Catalytic CO₂ Dry Reforming of Methane on Ni-Based Catalysts: A Review. *Fuel Process. Technol.* **2018**, *169*, 199–206. [[CrossRef](#)]
50. Siang, T.J.; Jalil, A.A.; Abdulrasheed, A.A.; Hambali, H.U.; Nabgan, W. Thermodynamic equilibrium study of altering methane partial oxidation for Fischer–Tropsch syngas production. *Energy* **2020**, *198*, 117394. [[CrossRef](#)]
51. Siang, T.J.; Jalil, A.A.; Liew, S.Y.; Owgi, A.H.K.; Rahman, A.F.A. A Review on State-of-the-Art Catalysts for Methane Partial Oxidation to Syngas Production. *Catal. Rev.* **2024**, *66*, 343–399. [[CrossRef](#)]
52. Irfan, M.; Li, A.; Zhang, L.; Javid, M.; Wang, M.; Khushk, S. Enhanced H₂ Production from Municipal Solid Waste Gasification Using Ni–CaO–TiO₂ Bifunctional Catalyst Prepared by Dc Arc Plasma Melting. *Ind. Eng. Chem. Res.* **2019**, *58*, 13408–13419. [[CrossRef](#)]
53. Osman, A.I. Catalytic Hydrogen Production from Methane Partial Oxidation: Mechanism and Kinetic Study. *Chem. Eng. Technol.* **2020**, *43*, 641–648. [[CrossRef](#)]
54. Luisetto, I.; Tuti, S.; Battocchio, C.; Lo Mastro, S.; Sodo, A. Ni/CeO₂–Al₂O₃ Catalysts for the Dry Reforming of Methane: The Effect of CeAlO₃ Content and Nickel Crystallite Size on Catalytic Activity and Coke Resistance. *Appl. Catal. A Gen.* **2015**, *500*, 12–22. [[CrossRef](#)]
55. Ma, R.; Xu, B.; Zhang, X. Catalytic Partial Oxidation (CPOX) of Natural Gas and Renewable Hydrocarbons/Oxygenated Hydrocarbons—A Review. *Catal. Today* **2019**, *338*, 18–30. [[CrossRef](#)]
56. Liu, T.; Snyder, C.; Veser, G. Catalytic Partial Oxidation of Methane: Is a Distinction between Direct and Indirect Pathways Meaningful? *Ind. Eng. Chem. Res.* **2007**, *46*, 9045–9052. [[CrossRef](#)]
57. Heitnes, K.; Lindberg, S.; Rokstad, O.A.; Holmen, A. Catalytic Partial Oxidation of Methane to Synthesis Gas. *Catal. Today* **1995**, *24*, 211–216. [[CrossRef](#)]
58. Nath, B.D.; Takaishi, K.; Ema, T. Macrocyclic Multinuclear Metal Complexes Acting as Catalysts for Organic Synthesis. *Catal. Sci. Technol.* **2020**, *10*, 12–34. [[CrossRef](#)]
59. Qiu, Y.; Chen, J.; Zhang, J. Effect of CeO₂ and CaO Promoters on Ignition Performance for Partial Oxidation of Methane over Ni/MgO–Al₂O₃ Catalyst. *J. Nat. Gas Chem.* **2007**, *16*, 148–154. [[CrossRef](#)]
60. Khoja, A.H.; Javed, A.H.; Naqvi, S.R.; Shakir, S.; Ud Din, I.; Arshad, Z.; Rashid, U.; Qazi, U.Y.; Naeem, N. Partial Oxidation of Methane over CaO Decorated TiO₂ Nanocatalyst for Syngas Production in a Fixed Bed Reactor. *Catalysts* **2022**, *12*, 1089. [[CrossRef](#)]

Disclaimer/Publisher’s Note: The statements, opinions and data contained in all publications are solely those of the individual author(s) and contributor(s) and not of MDPI and/or the editor(s). MDPI and/or the editor(s) disclaim responsibility for any injury to people or property resulting from any ideas, methods, instructions or products referred to in the content.